https://doi.org/10.5194/egusphere-2026-1336
Preprint. Discussion started: 13 March 2026

Observations of Coherent L-Band Emission from Snow-Covered Arctic Sea Ice

Ferran Hernández-Macià[1,2], Marcus Huntemann[3], Carolina Gabarró[1], Gunnar Spreen[3], and Randall K. Scharien[4]

[1]Barcelona Polar Lab (BPL), Institute of Marine Sciences (ICM-CSIC), Barcelona, Spain
[2]isardSAT, S.L., Barcelona, Spain
[3]Institute of Environmental Physics, University of Bremen, Bremen, Germany
[4]Department of Geography, University of Victoria, Victoria, BC, Canada

Correspondence: Ferran Hernández-Macià (fhernandezmacia@icm.csic.es)

Abstract. Radiometric measurements at L-band (1.4 GHz), collected in the Canadian Arctic in 2024, are used to study which type of model best reproduces the observations. While incoherent radiative transfer models are standard for sea ice thickness retrievals, they neglect phase interference effects. However, the observations analyzed here can only be explained when interference phenomena are explicitly included, requiring a coherent approach. To reduce uncertainties and ensure the robustness of the models, an optimal estimation method is used to determine snow and sea ice parameters consistent with the measured brightness temperatures and in situ measurements. The results show that the coherent model reproduces the observations substantially better than the incoherent formulation, yielding less than half the total cost with respect to the in situ measurements and being approximately 30,000 times more likely to explain the observations. These findings highlight the relevance of coherence effects at L-band, which are commonly neglected, at least in the context of local in situ measurements.

1 Introduction

Arctic sea ice extent and thickness have been declining rapidly (Perovich et al., 2020), with first-year ice now dominating, exhibiting thus a transition to younger, thinner ice (Meredith et al., 2019). Monitoring thin Sea Ice Thickness (SIT) is therefore essential for understanding these changes, and satellite-based SIT retrievals provide important insights into the state and evolution of this key variable. In particular, L-band radiometers, such as the European Space Agency (ESA) Soil Moisture and Ocean Salinity (SMOS) satellite (Kerr et al., 2010) and the NASA Soil Moisture Active Passive (SMAP) satellite (Entekhabi et al., 2010), have become indispensable for tracking thin ice because of their sensitivity to it. Particularly, due to the large penetration depth at this frequency, which allows for thickness retrieval up to approximately 1 m (Kaleschke et al., 2012). However, despite advances in algorithm development, significant uncertainties remain in modeling L-band emissions from snow-covered sea ice (Maass et al., 2015).

At L-band, SIT can be estimated up to a certain limit, ranging from a few centimeters to more than one meter, depending on the conditions, mainly temperature and salinity, and thus of the permittivity of the medium (Kaleschke et al. (2012), Hunte-

https://doi.org/10.5194/egusphere-2026-1336
Preprint. Discussion started: 13 March 2026

mann et al. (2014)). Electromagnetic waves propagating through ice and snow are subject to absorption and scattering between media layers, although the latter has proven to be negligible at this low frequency (Hernández-Macià et al., 2024). However, different radiative transfer models with distinct approaches differ in the computation of the sea ice brightness temperature (TB). For spatially homogeneous distinct layers with a thickness less than or similar to the wavelength of the electromagnetic radiation, coherence effects can influence the emitted radiation, eventually measured by the sensors. Previous attempts to tackle L-band sea ice emission modeling have mainly utilized an incoherent approach, i.e. neglecting the phase information and only consider power propagation. Current operational remote sensing products, such as the ESA's SMOS sea ice thickness product (Tian-Kunze et al., 2014), partially consider coherence effects within a semi-coherent model, accounting only for the interference between the sea ice top and bottom, ignoring the snow. Nevertheless, the effect of this features in the measured TB has been observed in previous works (Hallikainen (1983), St. Germain et al. (1993)). However, it remains unclear how this locally-observed coherence patterns can affect the TB measured in the satellite sensor's footprint of several kilometers. To this day, there are still only few observational datasets that clearly capture coherent signatures under well-characterized field conditions, so that their potential relevance for L-band sea ice emission remains insufficiently quantified and coherence is often neglected in practical modeling and further satellite retrievals.

In this work, data from the ARIEL L-band radiometer (Microwave Sensors and Electronics S.L.; Gabarró et al. (2022)) from a winter campaign in January 2024 at the Canadian High Arctic Research Station (CHARS, Cambridge Bay) is analyzed. Alongside the radiometric measurements, the sea ice and snow conditions were measured, allowing the possibility of understanding the observed TB. To interpret the data collected, the measurements are compared to coherent (Wilheit, 1978) and incoherent (Ulaby et al., 2014) radiative transfer models. However, to address possible input uncertainties coming from the in situ measurements, a method similar to an optimal estimation is used to assess the likelihood of the data being measured on the field.

2 Field study and data preparation

In January 2024, a joint campaign between the Institute of Marine Sciences (ICM-CSIC), the University of Bremen (UB), and the University of Victoria (UV) was conducted out of the Canadian High Arctic Research Station (CHARS), in Cambridge Bay, Canada. Among other measurements, the ARIEL L-band (1.4 GHz) radiometer was used to measure the TB of different snow-covered sea ice sites. This instrument is portable, allowing measurements at different surfaces. It has a opening angle of 36° in azimuth and 70° in elevation, mounted at 1-m height with respect to the surface, resulting in an estimated surface ellipsoidal-shaped footprint of 1.2 m in diameter. The setup for this experiment was the same as in the MOSAiC expedition, which is thoroughly described in Gabarró et al. (2022) and showed in Figure 1a. In this field campaign, the radiometer was deployed between the 17 and 25 January. The procedure was based in conducting several transects with multiple stops in which the radiometer measured the emission from the snow-covered sea ice, alongside other complementary measurements, such as ice auger drillings and ice corings and snow pit sampling to gain insight about the ground conditions.

https://doi.org/10.5194/egusphere-2026-1336
Preprint. Discussion started: 13 March 2026

(a) ARIEL L-band radiometer setup.

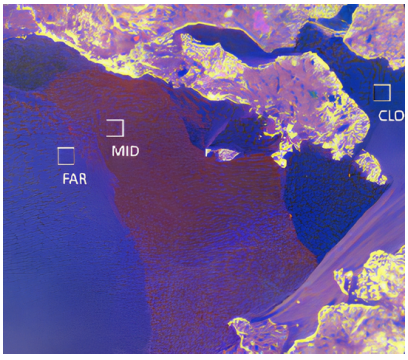

(b) RADARSAT Constellation Mission SAR image of the area where the field campaign was conducted, highlighting the three characterized sites: *CLO*, *MID*, and *FAR*. The false-color, based in backscatter for different SAR polarizations, is used for display (R=HH; B=HV; G=VV).

Figure 1. Overview and location of the sampled sites, alongside the ARIEL instrument setup.

All ARIEL measurements have been co-located with the ice thickness drillings and corings, and snow pits, thus obtaining the snow and ice conditions for each radiometer measurement. Particularly, ice drillings provide the snow and sea ice thickness', while ice cores deliver the same information in addition to the sea ice temperature and salinity. Finally, snow pits provide again the snow depth, but also its density, temperature and salinity. Overall, the encountered sea ice was thick (approximately $90 \pm 5\ cm$), and homogeneous around the different sites characterized. Contrarily, the snow depth and density presented much more variability, most likely driven by differences in wind and snowfall intensities, as well as through redistribution by wind within each site.

Figure 1b shows the location of the three sites that were sampled: *CLO*, *MID*, and *FAR*, named after the distance with respect to the base. A C-band frequency RADARSAT Constellation Mission SAR image of the area, acquired on 15 January 2024, shows how each site has a different backscatter response, which indicates that the ice at each site was grown at different times and under different conditions.

The sampled areas had an approximate length of about 1.5, 2.5, and 4 km for the *CLO*, *MID*, and *FAR* sites respectively. In order to characterize each sampled site, multiple co-located measurements were performed: for the *CLO* site, sixteen ice drillings, one ice core, and two snow pits; for the *MID* site, nine ice drillings, two ice cores, and four snow pits; and for the *FAR* site, four ice drillings, one ice core, and two snow pits. Specifically, sea ice thickness was higher and most variable at the *CLO* site, where the mean value reached $0.949 \pm 0.034\ m$. The *MID* site had thinner and more uniform ice, with a mean thickness

https://doi.org/10.5194/egusphere-2026-1336
Preprint. Discussion started: 13 March 2026

	CLO	MID	FAR
Site characteristics			
Sampled area length (km)	1.5	2.5	4.0
Co-located measurements			
Ice drillings	16	9	4
Ice cores	1	2	1
Snow pits	2	4	2
Sea ice thickness			
Mean (m)	0.949	0.867	0.858
Standard deviation (m)	0.034	0.018	0.018
Snow depth			
Mean (m)	0.073	0.087	0.077
Standard deviation (m)	0.036	0.045	0.043

Table 1. Summary of sampling sites (CLO, MID, and FAR) characteristics and measurements.

of $0.867 \pm 0.018\ m$. The *FAR* site showed slightly thinner ice, averaging $0.858 \pm 0.018\ m$. Snow depth patterns revealed even stronger spatial variability. At the *MID* sites, snow was thickest and most variable on average, with 0.087 ± 0.045. The *FAR* site followed closely with an average snow depth of $0.077 \pm 0.043\ m$. Meanwhile, the *CLO* site had a slightly lower snow depth and also less variability, averaging $0.073 \pm 0.036\ m$. The ice corings revealed that the ice salinity was high but homogeneous, while the temperature exhibited much more variability. This can be explained by the spatial variability of the snow depth that induces the thermal isolation of its ice underneath. This is summarized in Table 1.

Even though measurements were performed at multiple incidence angles with ARIEL, in this work only those done at 40° are considered, totaling thirty-five measurements. This selection is done because it matches the fixed incidence angle of SMAP. Furthermore, the TB intensity (first Stokes parameter, defined as $(TB_{\mathrm{H}} + TB_{\mathrm{V}})/2$) over sea ice is almost independent of incidence angle in the 0–40° range (Tian-Kunze et al., 2014), so fixing the angle does not strongly affect the total emission. In contrast, the polarization difference (PD) increases with incidence angle and is smallest near nadir, such that using a single oblique angle still allows us to capture a clear polarization split while keeping the geometry fixed and reducing the number of variables and associated uncertainties. The full multi-angle ARIEL dataset is used as a consistency check: the measured angular dependence of TB and PD follows the expected L-band signatures over sea ice (weak angular dependence of intensity and increasing PD with angle), which confirms the nominal operation of the instrument.

https://doi.org/10.5194/egusphere-2026-1336
Preprint. Discussion started: 13 March 2026

3 Emission modeling

The coherent model is based in Wilheit (1978), and hereafter it is called Wilheit model. This model uses wave-based radiative transfer for plane parallel layered media. Here, each layer is described only by its temperature and permittivity, so that scattering effects are not part of the model. An infinite number of reflections between the layers are considered. This is of importance specially when there is a thin layer of snow above the sea ice, as explored in Huntemann (2015). However, these effects can be rapidly vanish if there is roughness on any of the interfaces, i.e. air–snow, snow–ice, or ice–water, or spatial thickness variations across the instrument footprint exceeding the wavelength. Nevertheless, at L-band, the wavelength within the medium is greater than the typical small-scale roughness variations of the order of a few centimeters. Therefore, the roughness alone is not an argument for an incoherent treatment. The Wilheit model is particularly selected because it is the only coherent formulation that accounts for interference effects of the wave phase throughout the entire medium. The alternative option, the Microwave Emission Model of Layered Snowpacks (MEMLS, Wiesmann and Mätzler (1999)), incorporates interference only within very thin snow layers, after which coherence is effectively lost.

In order to compare the performance of the coherent model on matching the measured TB, an incoherent model (Ulaby et al. (1986), Gabarro et al. (2017)) is included in the study. This model is a simple implementation of a radiative transfer model considering also an infinite number of reflections between the layers, but neglecting the interference effects from the phase by using power instead of wave propagation. Like for the coherent model, a layered media of air-snow-ice-water is assumed, and the same variables and permittivity formulations are used.

In this work, the sea ice permittivity is modeled from the approximation described in Jones and Friedman (2000), specifically with the Maxwell-Garnett classical mean field theory. The brine inclusions trapped within the ice are assumed to be a randomly oriented ellipsoid with a given axis ratio, i.e. the ratio between the length (z-axis, major) and the width (x-axis, minor). Therefore, a higher axis ratio corresponds to a more elongated ellipsoid, approaching an infinite needle shape. Conversely, a small axis ratio indicates that the inclusion is more spherical when it is close to 1, whereas values approaching 0 imply an increasingly oblate shape, with 0 representing a disc of infinite extent. In this work, the axis ratio is transformed to logarithmic space to ensure positivity and better scaling. The shape of the brine inclusions is usually determined by the ice growth conditions, and this information is not a priori known. Needle-like inclusions can form under harsh ice formation conditions, whereas smoother conditions with minimal temperature fluctuations may produce spherical inclusions. A detailed analysis of the extreme cases can be found in Huntemann (2015) and Hernández-Macià et al. (2024). Since this permittivity formulation involves the mixing of two different substances, ice and brine, their permittivities are required. The permittivity of pure ice is thus modeled using the formulation proposed by Mätzler (2006), whereas the one for the brine comes from Stogryn and Desargant (1985). The real part of the complex permittivity for the snow layer is taken from Mätzler (1996), while its imaginary part is based on Tiuri et al. (1984) and Mätzler (2006). Finally, the complex permittivity of seawater is determined using the model from Klein and Swift (1977), assuming a standard Arctic Ocean salinity of 33.

https://doi.org/10.5194/egusphere-2026-1336
Preprint. Discussion started: 13 March 2026

To better disentangle the signal sensitivity to sea ice thickness from the simultaneous adjustment of multiple ice parameters, the role of the penetration depth (δ) can be explicitly analyzed. Temperature, salinity, and brine inclusion shape (through the axis ratio) jointly determine the complex permittivity of sea ice. This permittivity, in turn, controls two key radiative properties: the penetration depth, which governs from which depth most of the observed radiation originates and therefore when the TB becomes saturated with increasing thickness, and also the transmissivity at the snow-ice interface.

The penetration depth can be expressed as (Ulaby et al., 2014):

$$\delta = \frac{c}{\pi f} \frac{\sqrt{\epsilon'}}{\epsilon''}, \tag{1}$$

where c is the speed of light, f the frequency, and ϵ' and ϵ'' are the real and imaginary parts of the permittivity, respectively. Physically, δ corresponds to the depth at which the intensity of radiation propagating through the medium decreased by $1/e$. In practice, it provides an estimate of the thickness range over which T_B remains sensitive to changes in sea ice thickness before approaching saturation. By examining δ as a function of temperature, salinity, and axis ratio, it can therefore be illustrated how variations in these parameters modify the effective emission depth and, consequently, the sensitivity to ice thickness. Figure2 shows that the penetration depth exhibits a strong dependence on the brine inclusion shape throughout the temperature and salinity spectrum. Assuming spherical inclusions ($\alpha = 1$) leads to unrealistically large penetration depths at L-band, implying a delayed T_B saturation with thickness. In contrast, disc-shaped inclusions ($\alpha = 0.1$) or moderately prolate spheroids ($\alpha = 5$) produce comparable penetration depths, consistent with the reported L-band sensitivity to sea ice thickness up to approximately 1 m (Kaleschke et al., 2012). As the axis ratio increases further towards needle-like inclusions ($\alpha = 10$), δ decreases, reducing the effective emission depth and thus the thickness range over which T_B remains sensitive.

Regarding the sensitivity to snow layer thickness, Figure 3 presents the modeled TB as a function of snow depth. The snow density is fixed at 300 $\mathrm{kg\,m^{-3}}$, while the underlying sea ice thickness is kept constant at 0.9 m. Particularly, the solid line corresponds to a fixed incidence angle simulation, while the dashed line is the simulation integrated over the varying incidence angle within the ARIEL footprint weighted by the gaussian approximation of the antenna gain pattern ($\sigma = 14.87$ and $\sigma = 15.29$ for vertical and horizontal, respectively). The undulation of TB with increasing snow depth is caused by interference, reaching higher TB and also low PD at given snow path lengths, i.e. at certain snow depth and density. The output from the incoherent model is also shown in Figure 3 as a dotted line, result in an average of coherent model TB's, and not showing any sensitivity to the snow depth. The initial vertical dotted line connects the case of no snow cover, to a infinitesimal thin snow layer, which is an necessary artifact of an incoherent model. The undulation in the coherent simulations are stronger in TBH compared to TBV since a majority of the signal is transmitted without reflection.

4 Model-based optimization of measurements

Even though in situ data from the sea ice and snow conditions were collected throughout the campaign, there exist uncertainty regarding how these samples are representative of where the radiometer was measuring. The sea ice thickness was proven to

https://doi.org/10.5194/egusphere-2026-1336
Preprint. Discussion started: 13 March 2026

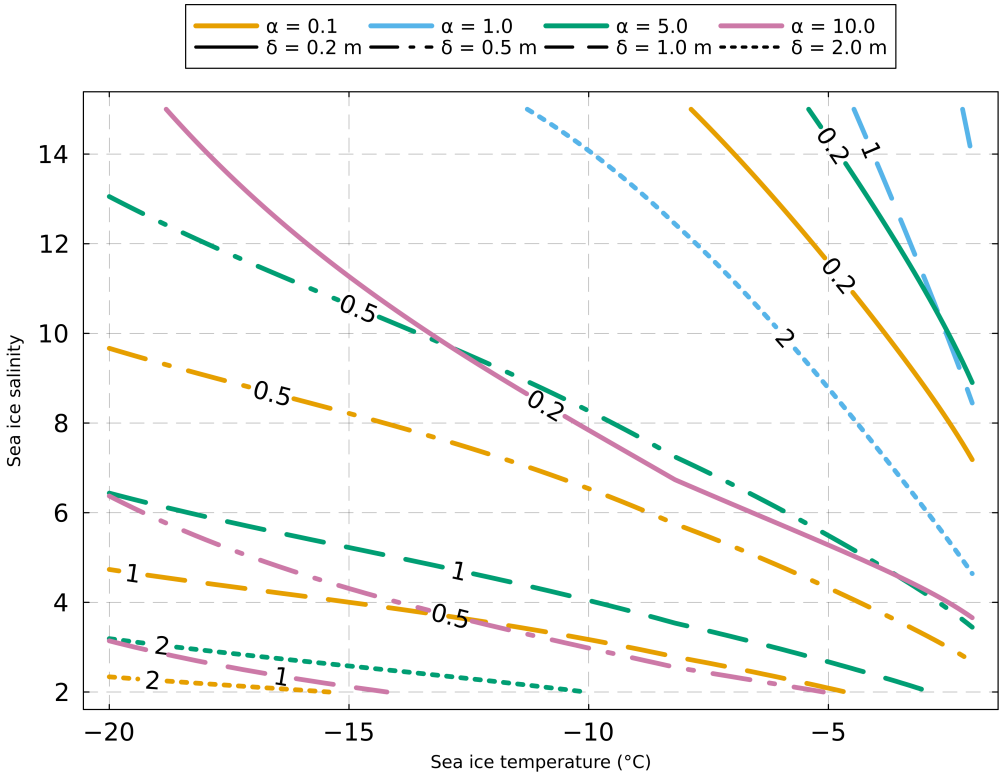

Figure 2. Penetration depth (δ) as a function of sea ice temperature and salinity for fixed axis ratios (α): 0.1 (disc, orange), 1 (sphere, blue), 5 (prolate spheroid, green), and 10 (needle, purple). Contours indicate selected thicknesses: 0.2 m (solid), 0.5 m (dash-dotted), 1 m (dashed), and 2 m (dotted).

be thick and homogeneous around, in the three different characterized regions. Similarly for the other sea ice conditions, i.e. salinity and temperature, there was no major distinction between the sites. However, the sea ice was grown at different times and under different conditions, so a difference in the permittivity could be expected due to the shape of brine inclusions within the ice, which was not measured. Another important source of uncertainty was the snow depth, since high variability was observed around within each site. This variability between different measurements is crucial to understand the observations, as TB is highly dependent on it, as shown in Figure 3.

To overcome this problem, a method similar to an optimal estimation framework is utilized. A cost function is minimized using the Nelder-Mead method (Gao and Han, 2012). Given the TB dependencies and the in situ measurements collected, six variables are optimized: snow depth (d_{snow}), snow density (ρ_{snow}), sea ice thickness (d_{ice}), sea ice temperature (t_{ice}), sea ice

https://doi.org/10.5194/egusphere-2026-1336
Preprint. Discussion started: 13 March 2026

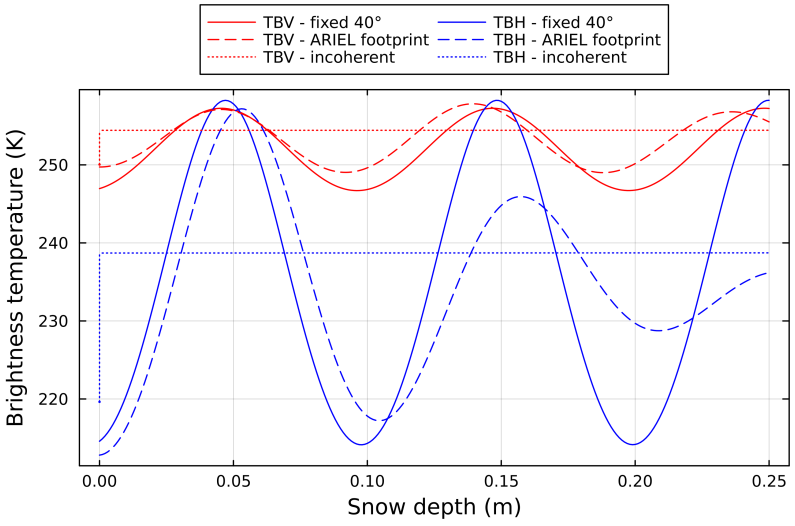

Figure 3. Brightness temperature as a function of the snow depth modeled with the Wilheit coherent model. The solid line is computed for a fixed incidence angle of $40°$, while the dashed is computed by integrating over the ARIEL's antenna pattern centered at $40°$ with surface homogeneity assumption. The dotted line shows the output of the incoherent model. The simulated conditions are: $T_{snow} = -15\,°C$, $\rho_{snow} = 300\,kg \cdot m^{-3}$, $d_{ice} = 0.9\,m$, $T_{ice} = -10\,°C$, $S_{ice} = 5$, $\alpha = 5$.

salinity (s_{ice}), and axis ratio (α). The latter is crucial for modeling the sea ice permittivity when the temperature and salinity conditions are fixed. Regarding d_{ice}, even though the encountered ice was almost 1 m thick and homogeneous, numerous works have shown its influence on the TB at L-band (Kaleschke et al. (2012), Tian-Kunze et al. (2014), Huntemann (2015)), thus justifying its inclusion in the optimization. The initial guesses for the optimization routine are taken from the in situ measurements that have more proximity in time and space. The objective function to be minimized is defined following the optimal estimation framework described by Rodgers (2000):

$$J(\mathbf{x}) = [\mathbf{y} - \mathbf{F}(\mathbf{x})]^T \mathbf{S}_\epsilon^{-1} [\mathbf{y} - \mathbf{F}(\mathbf{x})] + [\mathbf{x} - \mathbf{x}_a]^T \mathbf{S}_a^{-1} [\mathbf{x} - \mathbf{x}_a] \tag{2}$$

where $\mathbf{y} = [TB_H^{obs}, TB_V^{obs}]^T$ is the measurement vector containing the observed brightness temperatures from ARIEL. The state vector $\mathbf{x}$ consists of the six geophysical parameters retrieved in the optimization:

$$\mathbf{x} = [d_{snow}, \rho_{snow}, d_{ice}, t_{ice}, s_{ice}, \log_{10}\alpha]^T$$

The a priori state vector derived from the in situ measurements is $\mathbf{x}_a$. In fact, there is no fundamental difference in meaning between the left-hand side ($\mathbf{y}$) and the right-hand side ($\mathbf{x}$) of Eq. 2, as both the TBs and the geophysical variables represent measurements. The distinction lies solely in the space in which they are defined: $\mathbf{y}$ is expressed in TB space, whereas $\mathbf{x}$ resides in the state-parameter space, with the two connected through the corresponding forward models. $\mathbf{F}(\mathbf{x})$ is the forward radiative transfer model (coherent or incoherent) that maps the state vector to the observation space. Finally, $\mathbf{S}_\epsilon$ and $\mathbf{S}_a$ are the

https://doi.org/10.5194/egusphere-2026-1336
Preprint. Discussion started: 13 March 2026

covariance matrices representing the measurement and a priori uncertainties, respectively. These matrices are assumed to be diagonal, implying no correlation between the errors of the different variables, with the diagonal elements corresponding to the squared uncertainties (σ^2). In particular, an uncertainty of 5 K is assumed for both TB polarizations of the ARIEL instrument, as this constitutes a reasonable error budget that prevents the observations from driving the in situ measurements beyond their stated uncertainties. Adopting a larger value would effectively permit excessive deviations from the measurements, which is not desirable. For the snow and sea ice variables, the uncertainty is computed quantifying how certain we are about the in situ measurements. These can vary for each measurement depending on the observation conditions, e.g. time difference between ARIEL measurement and in situ observation, or distance to the ARIEL footprint and its homogeneity. Furthermore, the dispersion encountered in each particular site is also accounted, as well as the quantity of in situ measurements collected for each variable in each site characterized. Particularly, snow density has wide priors due the limited number of density samples collected, unlike snow depth measurements which were obtained from more frequent coring and drilling operations. As a result, most ARIEL measurements lack an associated density sample, leading to the assumption of a wide uncertainty for them. Regarding the axis ratio, which cannot be directly measured, the same prior and σ values are used across all sites and measurements.

5 Results and discussion

Eight separated simulations are performed, one for each time a site was characterized: *CLO*, *MID-1*, *MID-2*, and *FAR*, for both the coherent and the incoherent models. The MID site was sampled on two separate occasions with sufficient temporal separation to treat them as distinct sites. Table 2 summarizes the a priori values and uncertainties for the snow and ice parameters used in the optimization for each site. For each ARIEL measurement, the a priori values, i.e. the measurements that conform $\mathbf{x}_a$, are taken from the nearest co-located in situ sample. The uncertainties are assigned individually for each measurement based on the assessment of data availability and quality. The criteria is as follows: for snow depth, smaller uncertainties (0.005-0.01 cm) are assigned when multiple nearby drillings confirmed local conditions, while larger values (0.02 cm) are used when fewer and sparser samples are available. For snow density, uncertainties ranged from 25 kg m^{-3} when co-located snow pit data exists, to 100 kg m^{-3} when density information is sparse or extrapolated from distant locations. For sea ice thickness, uncertainties of 0.01 m are assigned when multiple drillings confirm homogeneity, increasing to 0.05 m when fewer measurements were available or greater spatial variability is observed. Regarding the sea ice conditions, temperature and salinity, constant priors are given for each site as only one ice cores was collected for each of them. Similarly, the uncertainty is fixed across measurements and sites, at 2 °C and 1.0, respectively. The brine inclusion axis ratio, which cannot be directly measured, is fixed at 5 ± 1.3 (equivalent to $\approx 0.7 \pm 0.1$ in logarithmic space), corresponding an intermediate prolate ellipsoidal shape and providing sufficient flexibility for the optimization to adjust within a physically plausible range under the observed conditions. Furthermore, this selection is motivated by the use of the single sea ice layer in the model, such that the resulting effective permittivity is intended to be representative of the entire ice column. In a more general framework, a multilayer ice representation with layer-dependent permittivity could be implemented to account for vertical variability within the ice.

https://doi.org/10.5194/egusphere-2026-1336
Preprint. Discussion started: 13 March 2026

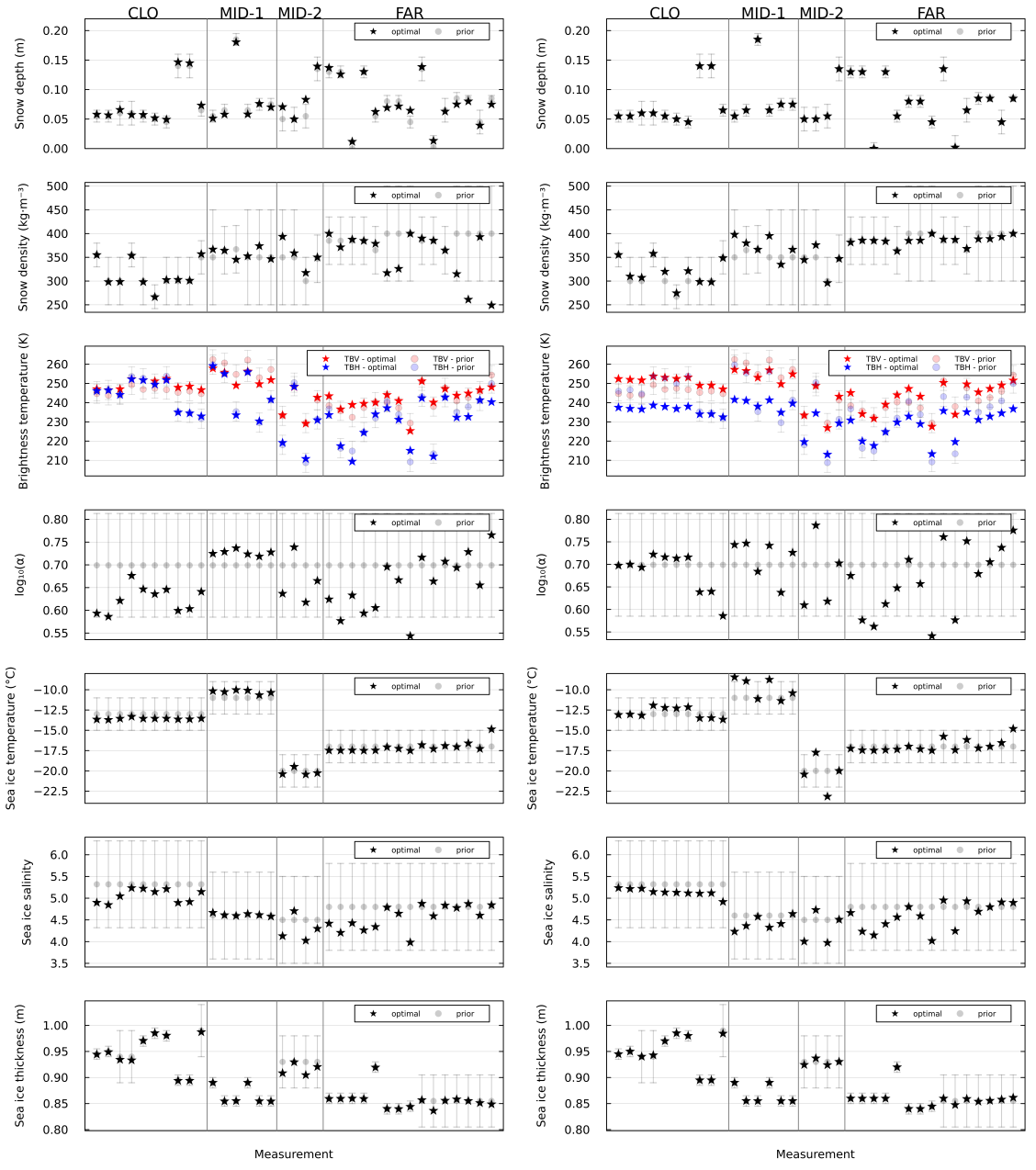

(a) Coherent model.

(b) Incoherent model.

Figure 4. Optimized snow depth, snow density, brightness temperatures TBH and TBV, axis ratio of the brine inclusions α, sea ice temperature, salinity, and thickness, for each measurement in each sampled site. The optimal values are shown as stars, while the measurements are shown in points with their uncertainties as error bars.

https://doi.org/10.5194/egusphere-2026-1336
Preprint. Discussion started: 13 March 2026

Parameter	CLO	MID-1	MID-2	FAR
Snow layer				
Snow depth (d_{snow}) [cm]	$4.50 - 14.00$	$5.50 - 18.50$	$5.00 - 13.50$	$0.00 - 13.50$
Uncertainty ($\sigma_{d_{\text{snow}}}$) [cm]	$0.01 - 0.02$	0.01	0.02	$0.005 - 0.02$
Snow density (ρ_{snow}) [kg m^{-3}]	$267 - 355$	$350 - 367$	$300 - 350$	$365 - 400$
Uncertainty ($\sigma_{\rho_{\text{snow}}}$) [kg m^{-3}]	$25 - 50$	$50 - 100$	$50 - 100$	$50 - 100$
Sea ice layer				
Sea ice thickness (d_{ice}) [m]	$0.895 - 0.99$	$0.855 - 0.89$	0.93	$0.84 - 0.92$
Uncertainty ($\sigma_{d_{\text{ice}}}$) [m]	$0.01 - 0.05$	0.01	0.05	$0.01 - 0.05$
Sea ice temperature (T_{ice}) [°C]	-13	-11	-20	-17
Uncertainty ($\sigma_{T_{\text{ice}}}$) [°C]	2	2	2	2
Sea ice salinity (S_{ice})	5.32	4.60	4.50	4.80
Uncertainty ($\sigma_{S_{\text{ice}}}$)	1.00	1.00	1.00	1.00
Brine inclusions axis ratio (α)	5.0	5.0	5.0	5.0
Uncertainty (σ_{α})	1.3	1.3	1.3	1.3

Table 2. A priori values and uncertainties for the snow and sea ice parameters used in the simulations.

The specific uncertainty assigned to each measurement is shown as error bars in Figure 4. Detailed prior values, uncertainties, and optimization settings are explicitly documented in the publicly available code repository (see *Code and data availability*).

Figure 4 shows the results of minimizing the objective function by simulating each measurement. It illustrates the variability of the optimized variables within each sampled site, along with their a priori values and σ bounds represented as error bars. Sea ice thickness shows almost no significant variation for neither of the models, as the measured ice was already quite thick, almost 1 m, resulting in no observable sensitivity (see Figure 2). There is also almost no variation between the prior and the optimized values for the sea ice temperature and salinity, even thought the incoherent model shows more variation as it relies on these variables, alongside the axis ratio, to change the permittivity trying to match the low PD of some measurements. For the same reason, the optimized axis ratio presents more variation for the incoherent model. Ultimately, the incoherent model has no sensitivity and thus no variation for the snow depth, while it shows changes in its density to better align with the observed TB. Contrarily, the coherent model is matching the observed TB by adapting snow depth and density, but despite that, the optimized values result quite close to the prior values and mostly within the uncertainty bounds.

Instead, TBH and TBV are shown to inform about how good the convergence of the simulation is. Almost all the differences are contained within $\pm 5\ K$ for the coherent model, with the major disparities corresponding to the vertical polarization. In fact, it is shown that the incoherent model is able to reasonably match those observations with higher PD, but it is totally unable to reproduce those with lower PD (it only matches TBV, but not TBH). Contrarily, the coherent model is matching TBH and TBV

https://doi.org/10.5194/egusphere-2026-1336
Preprint. Discussion started: 13 March 2026

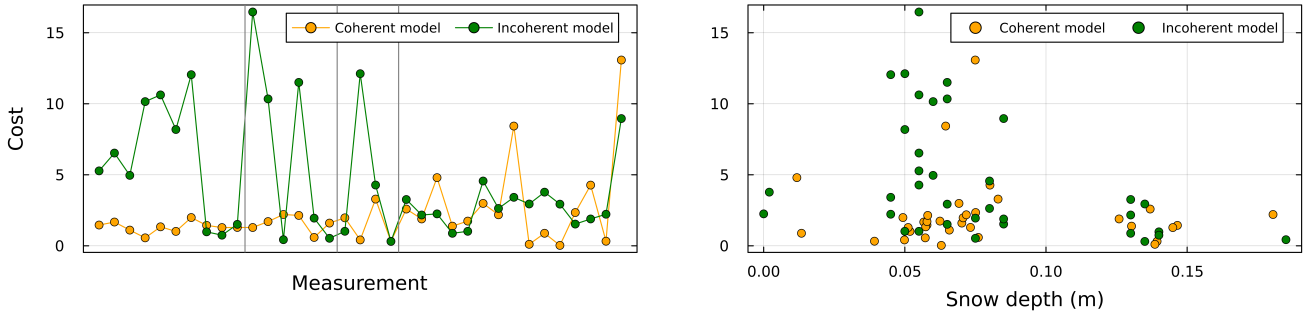

Figure 5. Left: Minimized cost for each measurement, for both the coherent and the incoherent models. Right: Minimized cost as a function of the optimized snow depth, for both the coherent and incoherent models.

for measurements with both higher and lower PD. Since the optimization is not artificially bounded, the optimal values can be outside the σ range, as it happens specially for the FAR measurements. The axis ratio, as expected, it exhibits the greatest dispersion. Ideally, there should be no dispersion in snow and ice conditions within a site, as the measurements were taken in close proximity. However, significant differences emerge, particularly in MID-2 and FAR, specially for the incoherent model. This aligns with the fact that these two sites exhibit greater uncertainty due to larger variations among the multiple samples taken within the same area, and that less ancillary co-located measurements were performed.

Figure 5 shows the minimized costs per measurement and also as a function of the optimized snow depth, for both the coherent and incoherent models. Overall, the coherent model keeps the cost per measurement considerably below the incoherent model, except for a few observations in *FAR*. When shown as a function of the snow depth, it is clearly shown that the coherent model presents lower costs throughout the snow depth range, and that the incoherent has substantially higher costs specially around 0.05 m, where the two polarizations are closer (see Figure 3). Computing the total minimized cost yields 75.72 for the coherent model, compared to 164.40 for the incoherent model. However, since the incoherent model has one fewer free parameter (due to its lack of sensitivity to snow depth), the Bayesian Information Criterion (BIC, Stoica and Selen (2004)) is used to determine the most suitable model. It can be computed as

$$BIC = \sum_{i=1}^{K} L_i + nKln(m), \tag{3}$$

where $K = 35$ is the number of observations, L_i is the cost per observation, n is the number of free parameters, and m is the total number of measurements (including all variables, i.e. $n+2$). Therefore, it results in $BIC_{coh} = 75.72+6\cdot35\cdot ln(8) = 512.40$ for the coherent, and $BIC_{inc} = 164.40+5\cdot35\cdot ln(8) = 528.30$ the incoherent model. Therefore, the analysis reveals a difference of $\Delta\text{BIC} = 15.9$ in favor of the coherent framework. The relative probability that the incoherent model is the correct one compared to the coherent model can be computed as $\exp(-\Delta\text{BIC}/2)$. This calculation results in a probability of 3.53×10^{-4}, indicating that the likelihood of the incoherent model explaining the observations is negligible compared to the coherent model,

https://doi.org/10.5194/egusphere-2026-1336
Preprint. Discussion started: 13 March 2026

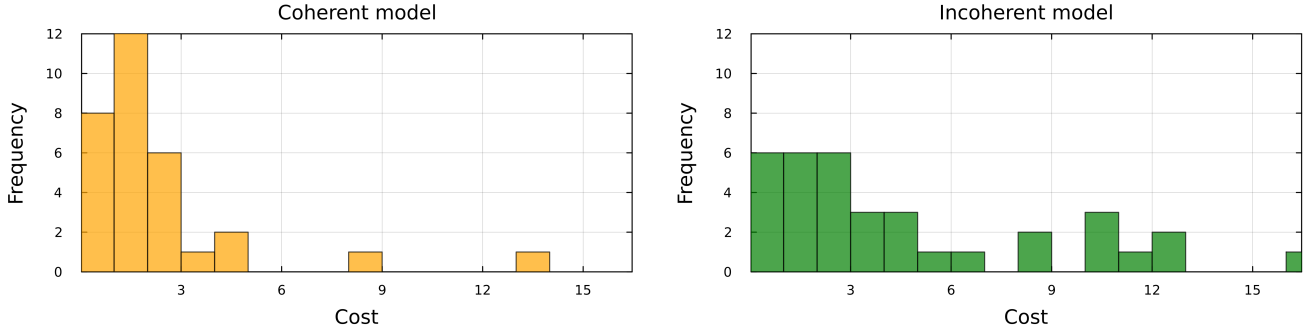

Figure 6. Left: Histogram of the minimized cost for each measurement for the coherent model. Right: Histogram of the minimized cost for each measurement for the incoherent model.

thus providing decisive statistical evidence for the latter. In other words, the coherent model is ≈ 30.000 times more likely to reproduce the in situ observations than the incoherent model. This is further illustrated in Figure 6, which presents a histogram of the minimized cost values for both the coherent and incoherent models. The incoherent model exhibits a more pronounced tail toward higher cost values, with several values extending well beyond 8–10 and even reaching the largest costs in the sample. In contrast, the coherent model shows a clear concentration of solutions at low cost values (predominantly below 3), and only a few cases exceeding 5. Overall, the distribution for the coherent formulation is more compact and skewed toward lower costs, indicating a systematically better fit to the observations.

To investigate how our observations fit, Figure 7 presents the results of the simulation by showing the TB modeled using the optimized variables for each measurement, for both the coherent and the incoherent models. Given that the TB is represented as a function of the snow depth, the deviation between the in situ and the optimized values is shown. The two upper plots (from the *CLO* and *MID-1* sites) show a good match between the coherent-modeled TB and the observations, while the incoherent model is not capable of reproducing the measurements with low PD. Furthermore, the dispersion between the TB simulations for each measurement in the same site is kept small, as well as the deviation between the a priori and the optimized snow depth values. This matches with the fact that for the *CLO* and *MID-1* sites there is more consistent information regarding the snow and sea ice conditions. For the *MID-2* site the results are less conclusive. Reasonable agreement is obtained for two points, particularly with the coherent model, whereas the remaining two points show substantial discrepancies. This behavior can be attributed to the limited snow depth information available at this site: although the coherent model is able to reproduce the observed TBs, the match is offset in terms of snow depth. Moreover, while a visual inspection might suggest that the incoherent model is closer to the observations, this apparent agreement arises from its lack of sensitivity to snow depth. As a result, the signal is not shifted, yet the TB values are still not properly reproduced. Finally, the last sampled site (*FAR*) presents the major dispersion in both the optimized TB and snow depth values. Similarly as for the previous site, the agreement is reasonable for most of the observations, while a few are shifted, and again this matches with having fewer measurements of the snow and sea ice conditions. It is worth noting that the two *FAR* points with lower snow depth correspond to snow removal experiments. As

https://doi.org/10.5194/egusphere-2026-1336
Preprint. Discussion started: 13 March 2026

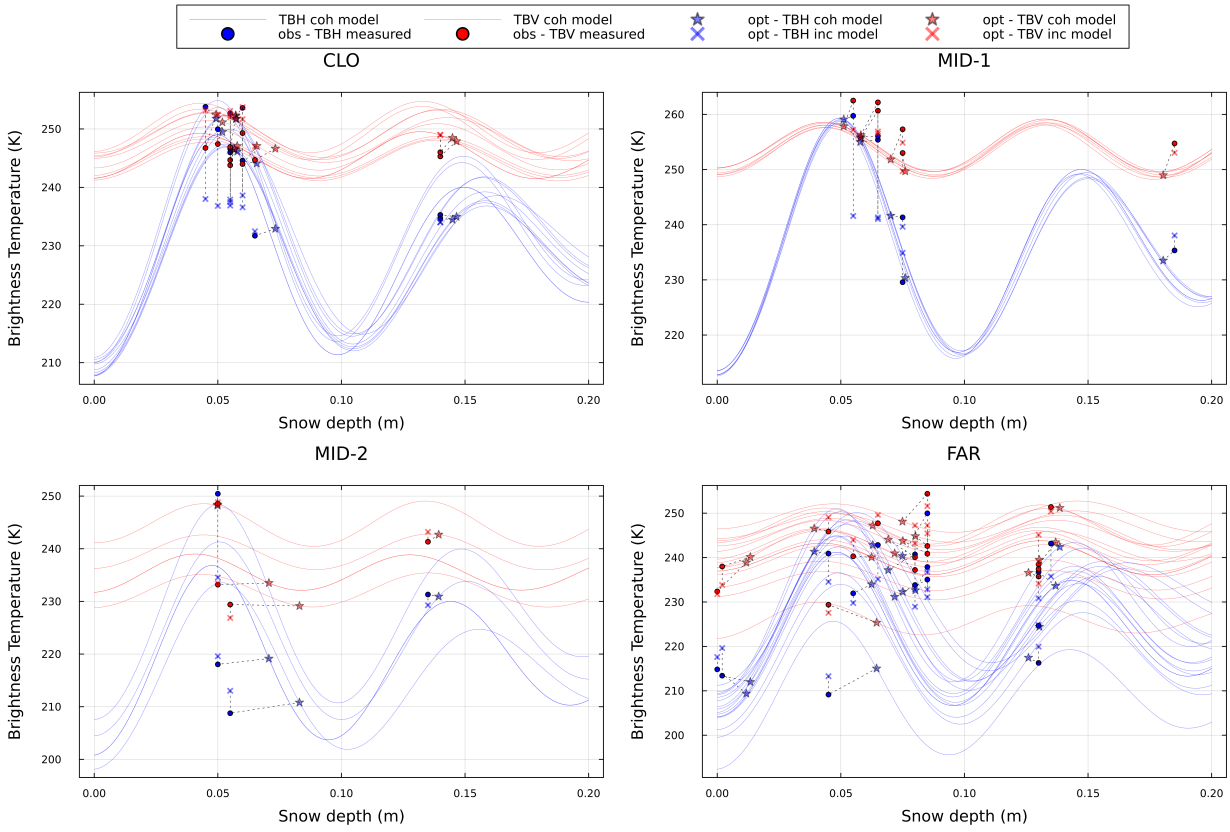

Figure 7. Measured brightness temperature as a function of the in situ measured snow depth (dot points, *obs - TBH/V measured*), alongside the brightness temperature modeled with the Wilheit coherent model computed with the optimized variables (star points, *opt - TBH/V coh model*), and the brightness temperature modeled with the incoherent model computed with the optimized variables (cross points, *opt - TBH/V inc model*). The dashed lines connect each three points that correspond to the same measurement. The continuous lines are the brightness temperature modeled with the coherent model using the optimized variables computed for a range of snow depths (*TBH/V coh model*).

shown, the measured TBs are reproduced by the coherent model with very small optimal snow depth values. Although the optimized depths are not exactly zero, they remain sufficiently low to be physically plausible, given that complete snow removal cannot be guaranteed during the experiments, particularly when accounting for possible contributions from the borders of the snow-free area.

It is worth noting that the assumption of small-scale homogeneous snow is necessary to preserve the coherent component of the signal generated at the snow–ice interface. Under this assumption, the wave reflected at the snow surface maintains its phase relationship with the upward emission from below, enabling interference between the two contributions. This homogeneity was visually confirmed during the field campaign, and refers to the footprint scale of the ARIEL sensor rather than to the broader

https://doi.org/10.5194/egusphere-2026-1336
Preprint. Discussion started: 13 March 2026

heterogeneity between the different stops within each site (CLO, MID, FAR). Coherent simulations already account for spatial averaging through the integration over incidence angles, and additional tests run with randomized snow depth perturbations of 1–2 cm show only minor impacts on the modeled brightness temperatures, so this extra variability was not further considered.

Besides that, sensitivity tests show that varying the a priori values within a reasonable range had little impact on the retrieved parameters, and, given that all priors except the axis ratio are based on in situ measurements, they can be considered sufficiently reliable. The optimized parameters mostly remained within their expected uncertainty ranges, indicating that the solution is physically plausible rather than an overfit to noise. For completeness, tests using an alternative global optimization method (Simulated Annealing) yield nearly identical optimal values, further supporting the robustness of the method.

Overall, the results strongly suggest that the coherent model is the only physical approach capable of matching the observations, since for the incoherent model the small PDs are not part of their solution space given the same input variables. Particularly, while the incoherent model show sensitivity to snow presence if thermodynamic correlations are considered (Maass et al., 2015), it fails to explain key features of the ARIEL measurements. Notably, the high TBH values observed cannot be explained under any circumstances by an incoherent model. The polarization split caused by the interface transition is too pronounced in such models, leading to TBH values that are significantly lower than the ARIEL measurements.

6 Conclusions

This study has demonstrated the effectiveness of a coherent radiative transfer model in modeling L-band radiometric observations of snow-covered Arctic sea ice collected during a winter field campaign at CHARS in January 2024. The measurements, obtained with the ARIEL portable radiometer at a fixed incidence angle of $40°$, have been analyzed together with in situ data on snow and sea ice conditions. The use of a coherent model, which incorporates interference effects at the snow-ice interface, successfully reproduced observed brightness temperatures and their low PDs. This contrasts with widely-used incoherent models, which neglect these effects and fail to explain the observed patterns.

The minimization of the cost function within the optimization, effectively allows the retrieval of the optimal state of all parameters involved, namely snow depth, snow density, sea ice thickness, sea ice temperature, sea ice salinity, and the brine inclusion axis ratio. This approach addressed uncertainties in the in situ measurements, providing optimized values that align with the observed TB. The results highlight snow conditions as a critical factor influencing TB variability due to coherence effects, with the most significant differences between in situ and optimized values occurring at sites with less a priori knowledge of the variables. The framework also confirmed the robustness of the coherent model, especially in measurements with certain snow conditions, around 5 cm, where interference effects are most pronounced.

The findings may have important implications for current and future satellite-based sea ice thickness products at L-band. The coherent effects observed in local ARIEL measurements could also influence the larger-scale footprints of satellites such as the current SMOS and SMAP, and also the future Copernicus Imaging Microwave Radiometer (CIMR) mission. However, these satellite sensors have footprint sizes in the order of 40 km and sub-footprint scale variability in the snow depth and ice

https://doi.org/10.5194/egusphere-2026-1336
Preprint. Discussion started: 13 March 2026

thickness below can average out the effects of thin snow. For homogeneous sea ice areas, for example for landfast ice, such coherence effects may be observed, in particular for early snow accumulation. Neglecting coherence effects from the snow cover could potentially alter the quality of current satellite retrieval during the early freeze-up at first snow accumulation.

Future research should focus on extending these findings to satellite footprints by conducting additional field campaigns in diverse Arctic regions. Such campaigns should aim to collect representative data on snow and sea ice conditions to further refine models and assess their scalability.

Code and data availability. The code for reproducing the analysis presented in this study is publicly available at https://github.com/ferranhema/coherent_emission-ariel. Both the in situ observations and optimization results are provided in the repository as CSV files. The ARIEL measured brightness temperature data used in the study is available open-access at Digital CSIC via https://doi.org/10.20350/digitalCSIC/17257.

Author contributions. Conceptualization, F.H.-M., M.H., C.G., G.S. and R.S.; methodology, F.H.-M., M.H., C.G., G.S. and R.S.; software, F.H.-M. and M.H.; validation, F.H.-M. and M.H.; formal analysis, F.H.-M. and M.H.; investigation, F.H.-M. and M.H.; resources, F.H.-M., M.H., C.G., G.S. and R.S.; data curation, F.H.-M., M.H., C.G., G.S. and R.S.; writing—original draft preparation, F.H.-M.; writing—review and editing, M.H., C.G., G.S. and R.S.; visualization, F.H.-M. and M.H.; supervision, M.H., C.G., G.S. and R.S.; project administration, C.G., G.S. and R.S.; funding acquisition, C.G., G.S. and R.S.. All authors have read and agreed to the published version of the manuscript.

Competing interests. No competing interests are present

Acknowledgements. This project is funded with the ARCTIC-MON project (PID2021-125324OB-I00) and also Programación Conjunta Internacional project called ICE-MOD, with reference PCI2019-111844-2, from the Agencia Estatal de Investigación in Spain. This work is supported by the Spanish government through the 'Severo Ochoa Centre of Excellence' accreditation (CEX2024-001494-S funded by AEI 10.13039/501100011033) to ICM-CSIC. Remote sensing data processing has been executed at the Barcelona Expert Center on Remote Sensing (BEC-RS, https://bec.icm.csic.es) of the Institut de Ciències del Mar ICM-CSIC. This work has been conducted in the framework of the PhD in Computer Science program of the Universitat Autònoma de Barcelona (UAB). This work is part of a Doctorat Industrial (AGAUR), with expedient number 2023 DI 0007. We acknowledge support from the Scientific Network PolarCSIC funded by the Consejo Superior de Investigaciones Científicas (CSIC), Spain. MH and GS acknowledge support from the ESA CIMR DEVALGO (contract no. 4000137493/22/NL/AD) and CIMR L2PAD (contract no. 4000143081/23/I-NS) studies. RS acknowledges support from the Natural Sciences and Engineering Research Council of Canada Discovery Grants Program (reference number: 110_2022_2023_Q1_2082).

https://doi.org/10.5194/egusphere-2026-1336
Preprint. Discussion started: 13 March 2026

References

Entekhabi, D., Njoku, E. G., O'Neill, P. E., Kellogg, K. H., Crow, W. T., Edelstein, W. N., Entin, J. K., Goodman, S. D., Jackson, T. J., Johnson, J., Kimball, J., Piepmeier, J. R., Koster, R. D., Martin, N., McDonald, K. C., Moghaddam, M., Moran, S., Reichle, R., Shi, J. C., Spencer, M. W., Thurman, S. W., Tsang, L., and Van Zyl, J.: The Soil Moisture Active Passive (SMAP) mission, Proceedings of the IEEE, 98 (5), 704–716, 2010.

Gabarro, C., Turiel, A., Elosegui, P., Pla-Resina, J. A., and Portabella, M.: New methodology to estimate Arctic sea ice concentration from SMOS combining brightness temperature differences in a maximum-likelihood estimator, The Cryosphere, 11, 1987–2002, https://doi.org/10.5194/tc-11-1987-2017, 2017.

Gabarró, C., Fabregat, P., Hernández-Macià, F., Jove, R., Salvador, J., Spreen, G., Thielke, L., Dadic, R., Huntemann, M., Kolabutin, N., Nomura, D., Hannula, H.-R., and Schneebeli, M.: First results of the ARIEL L-band radiometer on the MOSAiC Arctic Expedition during the late summer and autumn period, Elementa: Science of the Anthropocene, 10, https://doi.org/10.1525/elementa.2022.00031, 00031, 2022.

Gao, F. and Han, L.: Implementing the Nelder-Mead simplex algorithm with adaptive parameters, Comput Optim Appl, 5, 259–277, 2012.

Hallikainen, M. T.: A new low-salinity sea-ice model for UHF radiometry, International Journal of Remote Sensing, 4, 655–681, https://doi.org/10.1080/01431168308948581, 1983.

Hernández-Macià, F., Gabarró, C., Huntemann, M., Naderpour, R., Johnson, J. T., and Jezek, K. C.: On sea ice emission modeling for MOSAiC's L-band radiometric measurements, Annals of Glaciology, p. 1–14, https://doi.org/10.1017/aog.2024.38, 2024.

Huntemann, M.: Thickness retrieval and emissivity modeling of thin sea ice at L-band for SMOS satellite observations, Ph.D. thesis, 2015.

Huntemann, M., Heygster, G., Kaleschke, L., Krumpen, T., Mäkynen, M., and Drusch, M.: Empirical sea ice thickness retrieval during the freeze-up period from SMOS high incident angle observations, The Cryosphere, 8, 439–451, https://doi.org/https://doi.org/10.5194/tc-8-439-2014, 2014.

Jones, S. B. and Friedman, S. P.: Particle shape effects on the effective permittivity of anisotropic or isotropic media consisting of aligned or randomly oriented ellipsoidal particles, Water Resources Research, 36, 2821–2833, https://doi.org/https://doi.org/10.1029/2000WR900198, 2000.

Kaleschke, L., Tian-Kunze, X., Maaß, N., Mäkynen, M., and Drusch, M.: Sea ice thickness retrieval from SMOS brightness temperatures during the Arctic freeze-up period, Geophysical Research Letters, doi:10.1029/2012GL050916, 2012.

Kerr, Y., Waldteufel, P., Wigneron, J., Delwart, S., Cabot, F., Boutin, J., Escorihuela, M., Font, J., Reul, N., Gruhier, C., Juglea, S., Drinkwater, M., Hahne, A., Martin-Neira, M., and Mecklenburg, S.: The SMOS mission: New tool for monitoring key elements of the global water cycle, Proceedings of the IEEE IGARSS 2010, no. 5., 98, 666–687, 2010.

Klein, L. and Swift, C.: An improved model for the dielectric constant of sea water at microwave frequencies, IEEE Transactions on Antennas and Propagation, AP-25, 104–111, 1977.

Maass, N., Kaleschke, L., Tian-Kunze, X., and Tonboe, R. T.: Snow thickness retrieval from L-band brightness temperatures: a model comparison, Annals of Glaciology, 56, 9–17, https://doi.org/10.3189/2015AoG69A886, 2015.

Meredith, M., Sommerkorn, M., Cassotta, S., Derksen, C., Ekaykin, A., Hollowed, A., Kofinas, G., Mackintosh, A., Melbourne-Thomas, J., Muelbert, M., Ottersen, G., Pritchard, H., and Schuur, E.: Polar Regions. In: IPCC Special Report on the Ocean and Cryosphere in a Changing Climate, Cambridge University Press, Cambridge, UK and New York, NY, USA, pp. 203–320, https://doi.org/https://doi.org/10.1017/9781009157964.005, 2019.

https://doi.org/10.5194/egusphere-2026-1336
Preprint. Discussion started: 13 March 2026

Mätzler, C.: Microwave permittivity of dry snow, Geoscience and Remote Sensing, IEEE Transactions on, 34, 573 –581, https://doi.org/10.1109/36.485133, 1996.

Mätzler, C.: Thermal Microwave Radiation: Applications For Remote Sensing, publisher = Institution Of Electrical Engineers, 2006.

Perovich, D., Meier, W., Tschudi, M., Hendricks, S., Petty, A. A., Divine, D., Farrell, S., Gerland, S., Haas, C., Kaleschke, L., Pavlova, O., Ricker, R., Tian-Kunze, X., Webster, M., and Wood, K.: Arctic Report Card 2020: Sea Ice, Arctic Report Card, 2020.

Rodgers, C.: Inverse Methods for Atmospheric Sounding: Theory and Practice, Series on atmospheric, oceanic and planetary physics, World Scientific, ISBN 9789810227401, https://books.google.es/books?id=p3b3ngEACAAJ, 2000.

St. Germain, K. M., Swift, C. T., and Grenfell, T. C.: Determination of dielectric constant of young sea ice using microwave spectral radiometry, Journal of Geophysical Research: Oceans, 98, 4675–4679, https://doi.org/https://doi.org/10.1029/92JC02755, 1993.

Stogryn, A. and Desargant, G.: The dielectric properties of brine in sea ice at microwave frequencies, IEEE Transactions on Antennas and Propagation, 33, 523–532, https://doi.org/10.1109/TAP.1985.1143610, 1985.

Stoica, P. and Selen, Y.: Model-order selection: a review of information criterion rules, IEEE Signal Processing Magazine, 21, 36–47, https://doi.org/10.1109/MSP.2004.1311138, 2004.

Tian-Kunze, X., Kaleschke, L., Maaß, N., Mäkynen, M., Serra, N., Drusch, M., and Krumpen, T.: SMOS-derived thin sea ice thickness: algorithm baseline, product specifications and initial verification, The Cryosphere, 8, 997–1018, https://doi.org/10.5194/tc-8-997-2014, 2014.

Tiuri, M., Sihvola, A., Nyfors, E., and Hallikaiken, M.: The complex dielectric constant of snow at microwave frequencies, IEEE Journal of Oceanic Engineering,, 9, 377–382, https://doi.org/10.1109/JOE.1984.1145645, 1984.

Ulaby, F., Long, D., and of Michigan. Press, U.: Microwave Radar and Radiometric Remote Sensing, University of Michigan Press, ISBN 9780472119356, 2014.

Ulaby, F. T., Moore, R. K., and Fung, A. K.: Microwave Remote Sensing: Active and Passive, Addison-Wesley Publishing Company, Boston, USA, advanced Book Program / World Science Division, 1986.

Wiesmann, A. and Mätzler, C.: Microwave Emission Model of Layered Snowpacks, Remote Sensing of Environment, 70, 307–316, https://doi.org/https://doi.org/10.1016/S0034-4257(99)00046-2, 1999.

Wilheit, T. T.: Radiative Transfer in a Plane Stratified Dielectric, IEEE Transactions on Geoscience Electronics, 16, 138–143, https://doi.org/10.1109/TGE.1978.294577, 1978.